Vibrational spectroscopic studies on CO adsorption, NO adsorption CO + NO reaction on Pd model catalysts

Emrah Ozensoy and D. Wayne Goodman*

Department of Chemistry, Texas A&M University, P.O.Box 30012, College Station TX 77842-3012, USA. E-mail: goodman@mail.chem.tamu.edu

CO adsorption, NO adsorption and CO + NO reaction on various Pd model catalysts have been studied using vibrational spectroscopy from ultrahigh vacuum (UHV) up to elevated pressures ($\sim$1 bar) and the kinetics of the reaction compared with the conventional high surface area Pd/γ-Al$_2$O$_3$ catalysts. The structure sensitivity of the CO + NO reaction on different Pd surfaces is explained using Pd(111), Pd(100) single crystals and planar Pd/SiO$_2$/Mo(110), Pd/SiO$_2$/Mo(112), Pd/Al$_2$O$_3$/Ta(110) supported model catalysts by emphasizing the particle size/morphology effects and particle-support interactions. A reaction intermediate, isocyanate (–NCO), is detected *via in situ* vibrational spectroscopy at elevated pressures on Pd(111) single crystal surface and the significance of this reaction intermediate on the improvement of the catalytic NO$_x$ removal is discussed.

1. Introduction

In the early-1970's, acceptance of numerous environmental protection regulations world wide (such as the Clean Air Act in the U.S. in 1970) controlling the automobile exhaust emissions has brought about significant restrictions on the exhaust gases originating from mobile sources. Thus, increasingly stringent requirements for automobile emissions have created an intense scientific interest in the development of better catalytic conversion technologies which led to the Pt/Rh (90/10) three way catalysts (TWC) that simultaneously oxidize CO to CO$_2$, reduce NO$_x$ to N$_2$ and combust unburned hydrocarbons.[1] In the mid-1990's Pd-only TWC's that consist of Pd particles deposited on a high surface area metal-oxide support (typically γ-Al$_2$O$_3$) containing varying amounts of stabilizers and/or promoters such as CeO$_2$, SiO$_2$, La$_2$O$_3$, BaO were introduced as an alternative to Pt/Rh (90/10) catalyst and Pd rapidly became the most highly consumed precious metal by the automobile industry for emission control purposes.[2]

In order to design heterogeneous catalysts with higher performance, greater operational flexibility and long lasting efficiency, fundamental chemical and physical phenomena that take place on the active sites of the catalysts as well as on the catalyst supports must be understood at the molecular level. Toward achieving this challenging goal, properties of the Pd-based model heterogeneous catalyst systems for gas/solid interfaces have been studied intensively in our laboratories.[3–51] In particular, Pd single crystal surfaces[3–21] Pd/X bimetallic systems (X = Mo,[22–25] Ru,[26–29] Cu,[28,30] Ta,[25,29,31] W,[25,29,32,33] Re[25–27,29]), Pd/X/Y trimetallic systems (X/Y = Cu/Mo,[34] Au/Mo[34]), Pd clusters deposited on SiO$_2$,[10,35–41] Al$_2$O$_3$,[42–47] TiO$_2$[48–51] and MgO[49,51] have been investigated extensively using various surface analytical probes.

Vibrational spectroscopic techniques such as infrared reflection absorption spectroscopy (IRAS),[7,9,52–54,] polarization modulation infrared reflection absorption spectroscopy (PM-IRAS),[17,20,21,39,55] high resolution electron energy loss spectroscopy (HREELS),[56–60] sum frequency generation (SFG),[61] and their derivatives[62] have been exceptionally useful tools for elucidating the heterogeneous catalytic reaction mechanisms. These techniques provide the means for identification of active species on a catalyst surface with sub-monolayer accuracy and certain of these techniques (PM-IRAS and SFG) enable *in situ*

analysis of the catalysts under reaction conditions, in real time. In this report we present vibrational spectroscopic results from our laboratories relevant to the mechanism and kinetics of CO and NO adsorption and CO + NO reaction on Pd-based model catalysts including recent *in situ* PM-IRAS data acquired at elevated pressures.[17,20,21,39] The CO + NO reaction on Pd surfaces has also been a subject of interest in the literature. CO adsorption,[19,52,63–70] NO adsorption[56–58,71–87] and CO + NO reaction[21,88–109] on Pd-based catalysts have been examined experimentally and theoretically.[110–121]

This review is organized as follows: Section 2 details the experimental tools that have been used in our studies. Our approach to a fundamental understanding of complex surface reactions begins with simple, atomically well-defined model systems that can be investigated with atomic detail. The complexity is then increased to model systems with sufficient complexity to mimic many of the important aspects of a typical heterogeneous catalyst. Section 3 begins with a discussion of the adsorption behavior of each of the reactants of the CO + NO reaction on atomically well-defined Pd(100) and Pd(111) single crystal surfaces under both ultra high vacuum (UHV) and elevated pressure conditions ($\sim$450 Torr). Since it has been shown in our previous studies that Pd particles supported by SiO$_2$[37] and Al$_2$O$_3$[42] ultra-thin oxide films exhibit primarily $\langle 111 \rangle$ and $\langle 100 \rangle$ facets, Pd(111) and Pd(100) single crystal surfaces are addressed in detail. Next, moving to more complex systems, adsorption studies on Pd clusters deposited on planar ultra-thin oxide films such as SiO$_2$ and Al$_2$O$_3$ are examined focusing on particle size effects and particle-support interactions. Then IRAS results for CO + NO coadsorption and reaction on Pd(111) and Pd(100) single crystal model catalysts at low pressures (typically at $\sim$1 $\times$ 10^{-6} Torr) are presented and compared with similar experiments on Pd(111) at elevated pressure conditions ($\sim$180 Torr). In addition, pressure dependent formation of an isocyanate (–NCO) containing species on Pd(111) is discussed. This is followed by a discussion of the CO + NO reaction on planar, SiO$_2$-supported Pd model catalysts and the results compared with the single crystal data. Next, kinetics results for the CO + NO reaction on various Pd model catalysts and conventional Pd/Al$_2$O$_3$ high surface area powder catalysts with varying particle sizes are presented and the structure dependence of the reaction is

discussed in light of the vibrational and temperature programmed desorption (TPD) data. Finally, Section 4 provides a brief summary of the results.
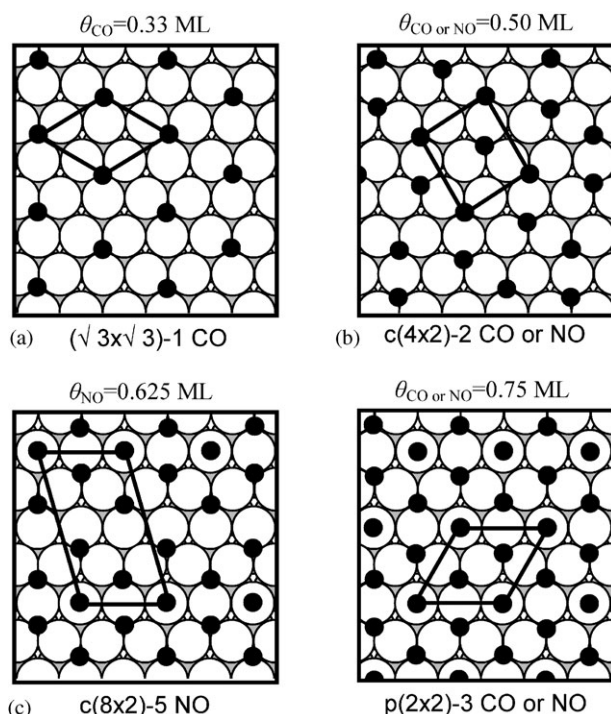
2. Experimental

Various surface analysis chambers have been utilized in the experiments described in this report. Typically these UHV systems were coupled to a micro-reactor for *in situ* vibrational spectroscopic and kinetic studies in addition to other standard surface science techniques such as infrared reflection absorption spectroscopy (IRAS), polarization modulation infrared reflection absorption spectroscopy (PM-IRAS), Auger electron spectroscopy (AES), X-ray and ultraviolet photoelectron spectroscopy (XPS and UPS), metastable impact electron spectroscopy (MEIS), low energy electron diffraction (LEED), high resolution electron energy loss spectroscopy (HREELS), temperature programmed desorption spectroscopy (TPD), scanning tunneling microscopy (STM), transmission electron microscopy (TEM) and gas chromatography (GC). For details about the preparation and experimental details of the model catalysts and the experimental methodologies described herein, the reader is referred to the relevant literature cited in the text.

3. Results discussion

3.1. CO adsorption on Pd single crystals

3.1.1. CO/Pd(111). Various coverage-dependent ordered overlayers of CO have been reported on Pd(111) single crystal surface (Fig. 1).[7,52,63,65] Vibrational spectroscopy, in particular the C–O stretching frequency for CO adsorbed on Pd single crystals, can be used for adsorption site assignments of ordered CO layers by comparing these values with the inorganic metal-carbonyl analogues where CO coordination to the metal center is known precisely. Although this methodology

has been criticized and shown to be misleading in some cases,[63,73,122] it has been found nevertheless to be very useful for many systems where site assignments *via* vibrational spectroscopy can be verified with other complementary methods.[52,123]

At a CO coverage of $\theta_{CO} = 0.33$ ML (ML = monolayer), recent STM studies reveal that a CO ordered overlayer with a $(\sqrt{3} \times \sqrt{3})R30°$–1CO structure is the dominant phase where CO resides primarily on 3-fold hollow sites.[65] Using the combination of LEED and IRAS it was shown that this CO overlayer yields a distinctly low C–O vibrational frequency of ~ 1850 cm^{-1} (Fig. 2)[7,52] When the CO coverage is increased to $\theta_{CO} = 0.50$ ML, the CO overlayer exhibits two coexisting c(4 × 2)–2CO phases where CO occupies either the bridging sites or threefold hollow sites.[65] This structure corresponds to a C–O vibrational frequency of ~ 1920 cm^{-1}.[7,52] Within $\theta_{CO} = 0.50$–0.75 ML, various complex overlayer structures are reported[65] yielding a CO vibrational band near 1965 cm^{-1}.[52] Recent STM experiments combined with density functional theory (DFT) calculations suggest that CO occupies primarily bridging sites on the Pd(111) surface within this coverage regime.[65] Finally at $\theta_{CO} = 0.75$ ML, saturation CO coverage is obtained yielding a (2 × 2)-3CO structure where CO resides on both atop and threefold hollow sites corresponding to vibrational features at 2110 and 1895 cm^{-1}, respectively.[7,52] The adsorption site assignments for CO/Pd(111) system at low pressures ($\sim 1 \times 10^{-8}$ Torr) that are mentioned above have been recently confirmed in combined STM and DFT studies of Rose and coworkers.[65]

CO adsorption system on Pd(111) was also investigated at elevated pressures using PM-IRAS20. PM-IRAS is a very versatile and a powerful *in situ* vibrational spectroscopic technique which can be used to analyze surface properties of gas/solid interfaces at pressures near one atmosphere with virtually no contribution from gas phase species.[17,20,21,39] In this recent study (see Fig. 2b)[20] it was demonstrated that CO overlayers follow similar trends with respect to the observed vibrational frequencies within the pressure range 10^{-6}–450 Torr (*i.e.* in a dynamic pressure range of nine orders of magnitude!), implying that no new pressure-induced species or adsorbate-induced surface reconstructions occur on the Pd(111) surface during CO adsorption at elevated pressures. Therefore an equilibrium phase diagram was constructed showing the various types of Pd(111) sites that are occupied by adsorbed CO molecules as a function of pressure and temperature. Furthermore, a transition from a phase dominated by CO molecules adsorbed on bridging sites to a different phase where CO resides on atop/threefold hollow sites is monitored by varying the CO pressure over nine orders of magnitude; an apparent activation energy of 44.3 kJ mol^{-1} was estimated from these PM-IRAS data for this phase transition.[20]

Fig. 1 Structures of the ordered overlayers that are formed during NO or CO adsorption on the Pd(111) single crystal surface (see text for details). (a) This structure is only observed for CO, NO forms a disordered phase at $\theta_{NO} = 0.33$ ML.[134] (b) A similar phase with bridging adsorption was also proposed for CO/Pd(111) at $\theta_{CO} = 0.33$ ML. (c) Complex overlayer structures were reported for CO/Pd(111) at this coverage where mostly bridging sites are occupied.[65]

3.1.2. CO/Pd(100). Similar to the CO/Pd(111) adsorption system, CO also exhibits almost identical vibrational features under low ($P_{CO} = 1 \times 10^{-6}$ Torr) and elevated pressure ($P_{CO} = 1$ Torr) conditions on Pd(100) (see Fig. 3a and 3b).[9] On the Pd(100) surface only bridged-site adsorption is observed over the entire coverage range ($\theta_{CO} = 0$–0.8 ML) where a single CO vibrational band shifts continuously from 1895 to 1995 cm^{-1}. At $\theta_{CO} = 0.5$ ML, CO forms an ordered overlayer structure of $(2\sqrt{2} \times \sqrt{2})R45°$–2CO[52] which corresponds to a C–O stretching frequency of 1950 cm^{-1}. At coverages higher than 0.5 ML, various incommensurate overlayers are observed due to uniaxial compression.[9,52] CO adsorption bands and adsorption site assignments for Pd(111) and Pd(100) single crystal surfaces at various CO surface coverages are summarized in Table 1.[124]

3766 *Phys. Chem. Chem. Phys.*, 2004, **6**, 3765–3778

This journal is © The Owner Societies 2004
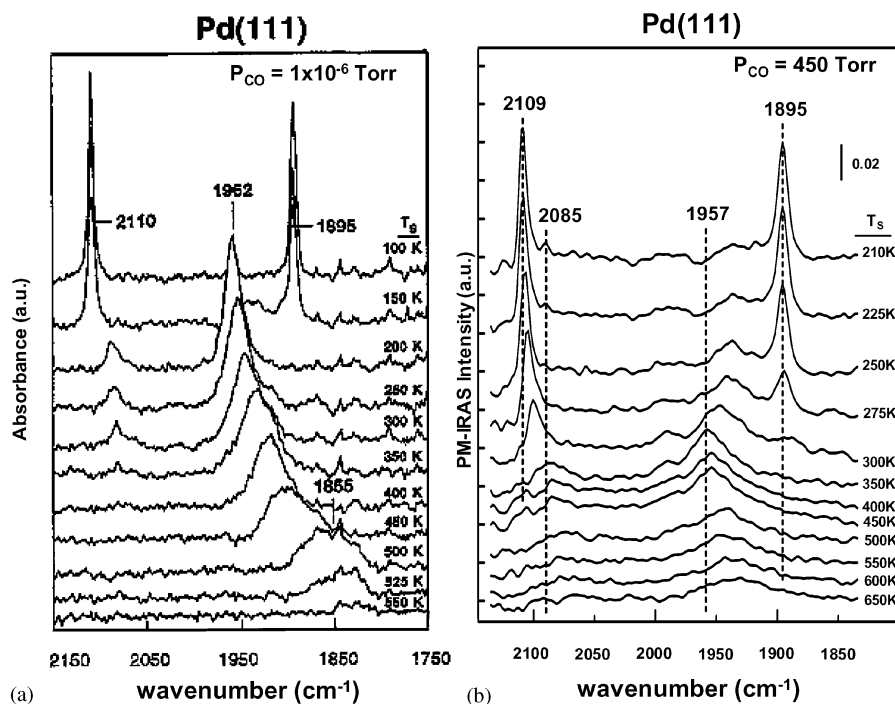
Fig. 2 *In situ* IRA spectra for CO adsorption on Pd(111) at $P_{CO} = 1 \times 10^{-6}$ Torr (a)[7] *in situ* PM-IRA spectra for CO adsorption on Pd(111) at $P_{CO} = 450$ Torr (b).[20] All of the spectra are acquired *in the presence of the CO gas phase*. Initial adsorption was performed at the highest temperature given in each of the spectral series.
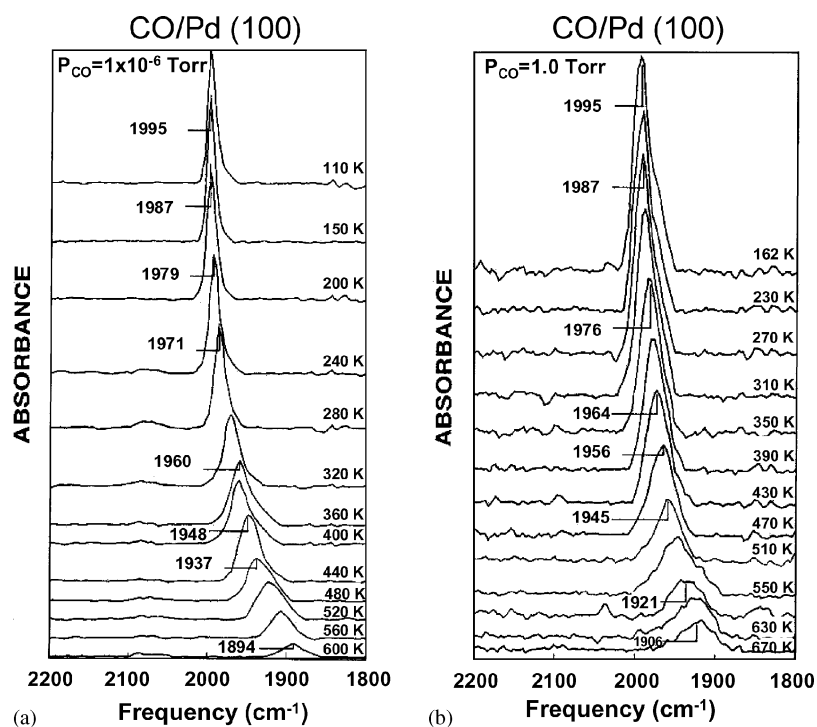
Fig. 3 *In situ* IRA spectra for CO adsorption on Pd(100) at $P_{CO} = 1 \times 10^{-6}$ Torr (a) at $P_{CO} = 1.0$ Torr (b).[9] All of the spectra are acquired *in the presence of the CO gas phase*. Initial adsorption was performed at the highest temperature given in each of the spectral series.

3.2. CO adsorption on Pd particles deposited on planar SiO₂ Al₂O₃ ultra-thin films

3.2.1. CO/Pd/SiO₂/Mo (110): CO adsorption at low pressures. Although, surface studies on single crystal model catalysts provide important clues about the reaction mechanism and kinetics, some of the very significant aspects of the conventional high surface area supported catalysts such as the particle size and morphology effects or particle–support interactions cannot be addressed using single crystals. A new approach has been developed in our laboratories to study metal particles on oxides that circumvents the major experimental drawbacks of bulk oxides by designing model catalysts consisting of metal particles (with controlled sizes) deposited on a metal-oxide ultra-thin film grown epitaxially on a conducting metal substrate.[125] Because vibrational spectroscopic techniques using probe molecules such as CO enable identification of particular binding sites on a catalyst surface, IRAS and PM-IRAS techniques were employed for supported metal particles.[35,37,39,126]

Table 1 ^{a}Site assignments for CO adsorption bs on Pd single crystals

θ(ML)	Pd(111)	υ_{CO}(cm^{-1})	Reference
Very low	Threefold hollow	1807	52
0.33	Threefold hollow	1848	52
0.50	Threefold hollow	1920	63
0.65	Bridge	1966	52
0.75	Threefold hollow/atop	1894	7, 9, 52
		2110	

θ(ML)	Pd(100)	υ_{CO}(cm^{-1})	Reference
Very low	Bridge	1807	9, 52
↓	↓	↓	
0.81	Bridge	1997	

^{a} Reproduce from Ref. 124 with permission.

IRAS results for CO adsorption on Pd particles with various particle sizes deposited on an *amorphous* SiO$_2$ ultra-thin films grown on Mo(110) is given in Fig. 4.[35,37] Fig. 4a clearly shows that CO adsorption features for Pd particles supported on a planar SiO$_2$ film can be explained readily using CO/Pd(111) and CO/Pd(100) data. Three major vibrational features are visible for the saturation coverage of CO at 100 K in all of the spectra in Fig. 4a. IR bands at 2110 and 1895 cm^{-1} correspond to CO molecules adsorbed on atop and threefold hollow sites on ⟨111⟩ facets of the Pd particles, respectively, whereas the band at 1995 cm^{-1} corresponds to CO molecules residing on the bridging sites of ⟨100⟩ facets. Fig. 4a also presents an important aspect regarding the change in the morphology of the Pd particles as a function of the particle size. Different catalysts with Pd particle sizes of ∼5nm (θ_{Pd} = 1 ML), 15 nm (θ_{Pd} = 7 ML) and >20 nm (θ_{Pd} = 15 ML), determined by STM and chemisorption methods are investigated in Fig. 4a.[37] As the Pd particle size decreases, CO stretching bands in the IRA spectra become broader due to the increasing number of defect sites (such as edges or kinks) and disorder on the smaller particles.

Fig. 4b[35] presents the CO adsorption behavior of silica supported Pd particles (θ_{Pd} = 15 ML) with varying temperature. Similar to the single crystal Pd surfaces (see Figs. 2 and 3), at low CO coverages (above 350 K) vibrational features (1830–2000 cm^{-1}) that are characteristic of multiply coordinated CO molecules on bridging and threefold hollow sites are observed on silica supported Pd particles while at high CO coverages adsorption at atop sites (2110 cm^{-1}) is also visible in addition to some bridging (1995 cm^{-1}) and threefold hollow (1895 cm^{-1}) adsorption sites.

Fig. 4c[37] shows the structural and morphological changes of the silica supported Pd particles (θ_{Pd} = 15 ML) with pre-annealing temperature. All IRA spectra in Fig. 4c were obtained at 100 K for Pd particles (θ_{Pd} = 15 ML) deposited at 100 K. After the Pd deposition at 100 K, the model catalysts were annealed to the given temperatures then dosed with 1 × 10^{-6} Torr CO. It is apparent that pre-annealing the Pd particles has a significant effect on the width of the CO adsorption bands indicating that the Pd particles exhibit more ordered facets with increasing pre-annealing temperatures. Fig. 4c illustrates the relative low mobility of the Pd particles on the *amorphous* SiO$_2$ film at low temperature whereas the growth of Pd clusters with ordered facets presents a kinetic barrier which can be overcome by pre-annealing the Pd particles to higher temperatures.[37] The IRAS data indicate that Pd clusters supported on amorphous SiO$_2$ consist primarily of ⟨111⟩ and ⟨100⟩ facets, with the most stable surface structure suggested to be cubo-octahedral geometry.[37] Recent STM experiments[80,124,127] on Pd particles deposited on planar SiO$_2$ and Al$_2$O$_3$ surfaces have confirmed that the Pd particles have a truncated-octahedral geometry, the so-called "*Wulff polyhedron*".[128]

3.2.2. CO/Pd/SiO$_2$/Mo(112): CO adsorption at elevated pressures. Recently a method for synthesizing *crystalline* SiO$_2$ ultra-thin films on Mo(112) has been developed in our laboratories[40,41] by slightly modifying the approach used by Freund
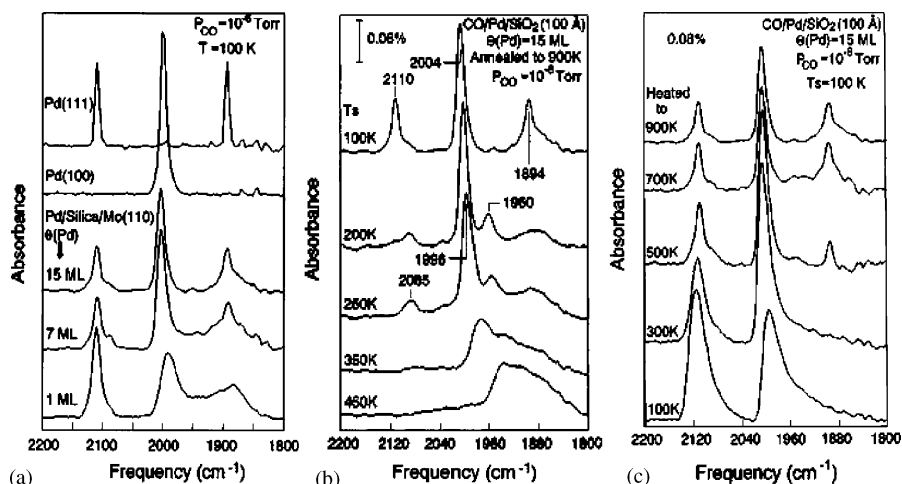
Fig. 4 (a) IRA spectra for CO adsorption on Pd/SiO$_2$/Mo(110) surface at 100 K with varying Pd coverages of 1, 7, 15, ML in comparison with Pd(111) Pd(100) surface (Pd particles were ordered by pre-annealing to 900 K prior to CO adsorption).[37] (b) Effect of temperature on the CO adsorption on Pd(θ_{Pd} = 15 ML)/SiO$_2$/Mo(110).[37] (c) IRAS for CO adsorption on Pd(θ_{Pd} = 15ML)/SiO$_2$/Mo(110) acquired at 100K after pre-annealing the Pd particles to the given temperatures.[35] All of the spectra in (a)–(c) were obtained in the presence of P_{CO} = 1 × 10^{-6} Torr.

and coworkers.[124,129,130] The primary advantage of employing crystalline oxide thin films rather than amorphous films for investigating model heterogeneous catalysts is the fact that on the crystalline oxide surfaces, morphological changes of *both* the oxide surface and the metal particles can be studied with scanning probe techniques such as STM with atomic resolution whereas on the amorphous oxides, surface roughness and disorder prevent one from obtaining detailed information about the oxide support.

The top image in Fig. 5a[39] presents the atomically resolved STM image of a crystalline SiO$_2$ ultra-thin film grown on a Mo(112) substrate. This high resolution STM image shows that SiO$_2$ film obtained with the preparation method employed here is atomically flat and exhibits a homogeneous c(2 × 2) structure with a unit cell spacing of ~0.5 nm that is consistent with previous LEED studies[130] for crystalline SiO$_2$ surfaces. In addition, recent ultraviolet photoelectron spectroscopic (UPS) and metastable impact electron spectroscopic (MIES) studies in our laboratories reveal that SiO$_2$ films grown with this method yield a band gap of 8.8 eV.[131] This value is in excellent agreement with bulk SiO$_2$, indicating that these SiO$_2$ thin films present a good model for a high surface area SiO$_2$ support in terms of their electronic structure. The STM image at the bottom of Fig. 5a shows the morphology of the Pd particles ($\theta_{Pd} = $ ~4 ML) deposited on a crystalline SiO$_2$ thin film. According to the STM results in Fig. 5a, Pd nano-particles have an average diameter and height of 3.5 and 0.7 nm, respectively. Furthermore, temperature dependent STM studies[39–41] indicate that no significant morphological changes are observed for Pd particles supported by *crystalline* SiO$_2$ upon annealing to 700 K in vacuum whereas annealing to temperatures above 700 K leads to sintering and inter-diffusion of the Pd particles and formation of Pd-silicide.[40,41]

The PM-IRAS technique was applied to three-dimensional structures (in this case silica supported Pd nano-clusters) for the first time in our laboratories to study the catalytic behavior of these surfaces at elevated pressures.[39] PM-IRAS data for CO adsorption on crystalline silica supported Pd particles with an average diameter of 3.5 nm at 185 Torr is shown in Fig. 5b and compared with CO adsorption at 133 mbar on Pd(111) (Fig. 5c).[39] When the topmost spectrum in Fig. 5b, obtained at 300 K, is compared with the spectrum obtained at 300 K in Fig. 5c, it can be readily seen that the prominent features in both of these spectra are the CO adsorption bands centered at 2089 and 1957 cm^{-1} indicating that the silica supported Pd particles studied here exhibit mostly ⟨111⟩ facets. In addition to these adsorption bands, a small feature located at 2009 cm^{-1} in the topmost spectrum of Fig. 5a is also visible and corresponds to CO adsorbed at bridging sites of ⟨100⟩ facets.

Temperature dependent reversibility of CO adsorption on crystalline SiO$_2$ supported Pd particles at elevated pressures has also been investigated[39] (Fig. 6a). It was observed that annealing Pd particles in the presence of the high pressure CO background ($P_{CO} = $ 185 mbar) and cooling to 300 K leads to irreversible changes in the PM-IRA spectra. Contrary to the crystalline SiO$_2$ supported Pd particles, CO adsorption on Pd(111) at $P_{CO} = $ 133 mbar is totally reversible (Fig. 6b). It should be noted that the temperature dependent STM experiments[39] show that Pd particle morphology is invariant to temperature variations between 300–700 K. The changes observed in PM-IRAS data cannot be attributed to reconstruction of the Pd particles but rather has been shown to be caused by C deposition on the Pd particles after annealing. Subsequent AES (see inset of Fig. 6a)[39] data confirm that CO dissociation takes place on the small Pd particles at elevated pressures and temperatures ($T > $ 600 K) and leads to poisoning of the CO adsorption sites on the supported Pd nano-clusters. CO dissociation on oxide supported small Pd particles have been also reported for Pd/SiO$_2$ high surface area powder catalyst[132] and Pd/Al$_2$O$_3$/Ta(110) planar model catalysts.[42] On the other hand, reversibility of the CO adsorption with temperature on Pd(111) single crystal surface reveals that C–O bond scission does not occur on atomically flat Pd(111), therefore the active sites for CO dissociation are likely the defect/edge sites on Pd nano-clusters.

3.2.3. CO/Pd/Al$_2$O$_3$/Ta(110): influence of the oxide support.

In order to study the effect of the oxide support on the adsorption properties of the deposited metal particles, model catalysts consisting of Pd nano-clusters supported by planar (amorphous) Al$_2$O$_3$ oxide surfaces grown on Ta(110) were also studied using IRAS.[42,44,46,126,133] Model catalysts with various Pd particle sizes were prepared and the average Pd particle sizes were determined by TEM (for the TEM experiments Pd/Al$_2$O$_3$/C samples were prepared by employing similar methods on carbon-covered molybdenum grids).[42]

Fig. 7 presents the IRAS data for CO adsorption at 1×10^{-5} Torr on Pd/Al$_2$O$_3$/Ta(110) planar model catalysts with different particle sizes. According to the TEM results, model catalysts with Pd loadings of $\theta_{Pd} = $ 1 ML and $\theta_{Pd} = $ 5 ML correspond to average particle sizes of ~2.5 and ~7 nm, respectively.[42] From a general point of view, CO adsorption bands for Al$_2$O$_3$ supported Pd particles (Figs. 7a and 7b7)
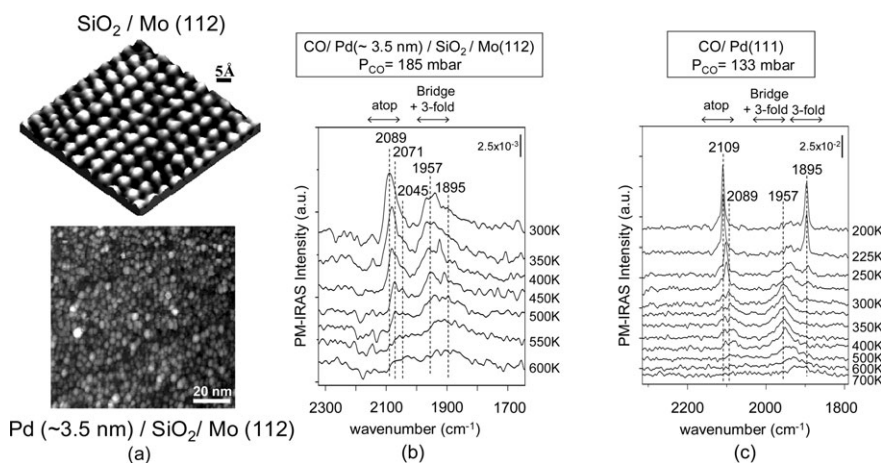
Fig. 5 (a) High resolution STM image for crystalline SiO$_2$ film grown on Mo (112) substrate (top) STM image for Pd particles with an average diameter of 3.5 nm deposited on crystalline SiO$_2$ thin film support (bottom).[39] (b) PM-IRAS for CO adsorption on Pd (3.5 nm)/SiO$_2$/Mo (112) at 185 mbar (140 Torr).[39] (c) PM-IRAS for CO adsorption on Pd(111) at 133 mbar (100 Torr).[20]
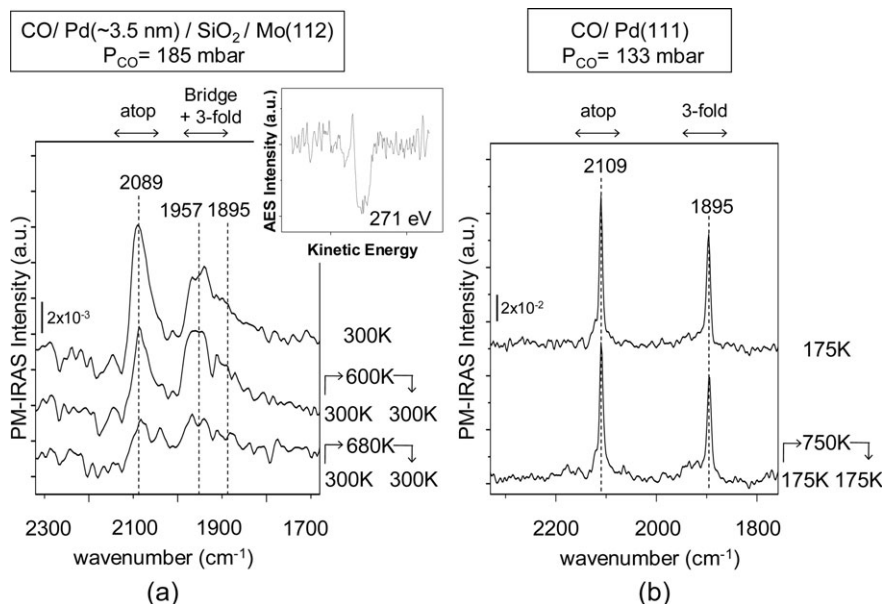
Fig. 6 Reversibility/irreversibility of the CO adsorption bands at elevated pressures for (a) Pd(3.5 nm)/SiO$_2$/Mo(112) and (b) Pd(111). Initial adsorption was performed at a low temperature (300 K for (a), 175 K for (b)). Pd surfaces were annealed to the given temperatures in the presence of CO subsequently cooled down to the initial adsorption temperatures where PM-IRAS data were acquired. Inset in (a) presents the difference between the AES for clean C and deposited Pd particles.[39]
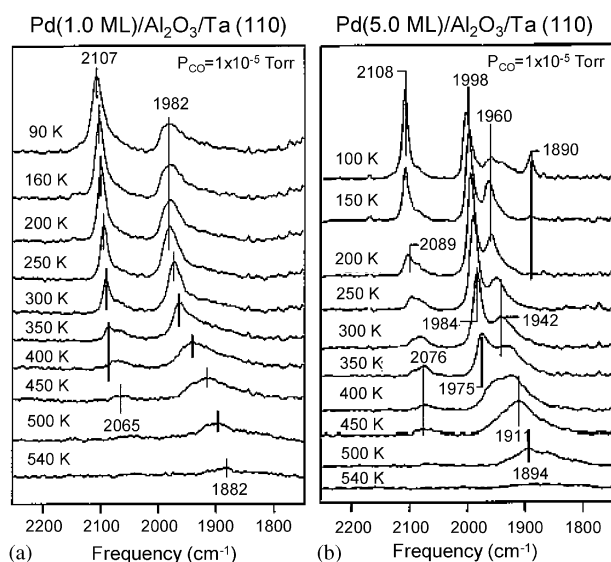
Fig. 7 IRA spectra for CO adsorption on Pd/Al$_2$O$_3$/Ta(110) with Pd coverages of 1.0 ML (a) and (b) 5.0 ML at various temperatures. Spectra were obtained for catalyst surfaces in equilibrium with CO ($P_{CO} = 1 \times 10^{-5}$ Torr).[42]

show significant similarities to CO vibrational bands for SiO$_2$ supported Pd particles with comparable particle sizes (Fig. 4a). As in the case of SiO$_2$ supported Pd particles, when a Pd/Al$_2$O$_3$/Ta(110) model catalyst is exposed to $P_{CO} = 1 \times 10^{-5}$ Torr until the saturation coverage is obtained at 100 K, vibrational features corresponding to CO species residing on the atop (2108 cm^{-1}), bridging (1960 cm^{-1}) and threefold hollow (1890 cm^{-1}) sites of ⟨111⟩ facets as well as CO molecules occupying bridging (1998 cm^{-1}) sites of ⟨100⟩ facets of the Pd particles are observed. As the temperature is increased, decreasing CO coverage on the Al$_2$O$_3$ supported Pd particles leads to the gradual depopulation of the atop sites while multiply coordinating bridging and threefold hollow sites are still significantly populated.

Besides these similarities, there exist some disparities for CO adsorption bands on Pd nano-particles of comparable sizes on

SiO$_2$ and Al$_2$O$_3$ model catalysts that are related to the slight differences in the morphology of the Pd particles on these two different oxide surfaces. Comparison of the topmost spectrum in Fig. 7b for the saturation coverage of CO at 100 K on Pd/Al$_2$O$_3$/Ta(110) corresponding to an average Pd particle size of ∼7 nm with the bottommost spectrum in Fig. 4a obtained for the saturation coverage of CO at 100K on Pd/SiO$_2$/Mo(110) surface with an average Pd particle size of ∼5 nm highlights this disparity. It is apparent that the CO adsorption features for the Al$_2$O$_3$ supported Pd particles are better resolved and display a narrower line width with respect to the SiO$_2$ supported Pd particles of comparable size. This indicates that ⟨111⟩ and ⟨100⟩ facets existing on the Al$_2$O$_3$ supported Pd particles are more ordered than the SiO$_2$ case. This is consistent with the recent STM studies on Pd/Al$_2$O$_3$/NiAl(110)[127] and Pd/SiO$_2$/Mo(112)[39,124] suggesting that Pd particles on the crystalline Al$_2$O$_3$ support exhibit very well defined ⟨111⟩ and ⟨100⟩ facets and a truncated cubo-octahedral geometry with sharp, flat edges whereas on the crystalline SiO$_2$ support, the Pd clusters are relatively less ordered.

Particle size effects are also seen for the Pd/Al$_2$O$_3$/Ta(110) system when IRAS data for CO adsorption on Pd particles with various sizes are considered. As it was seen in the SiO$_2$ case, on Al$_2$O$_3$ smaller Pd particles (θ_{Pd} = 1 ML) in Fig. 7a lead to broad CO adsorption bands whereas larger Pd particles (θ_{Pd} = 5 ML) in Fig. 7b result in well-resolved sharp features in IRA spectra for adsorbed CO. This is again in good correlation with the argument suggesting that small Pd particles supported by oxides exhibit a higher density of defects and disorder with respect to larger particles. Furthermore some other implications of higher defect/edge density on the smaller Al$_2$O$_3$ supported Pd particles can be also recognized by considering the larger atop/bridging intensity ratio for the smaller particles and the lack of well resolved threefold hollow adsorption bands (Fig. 7a and 7b). In addition, the phase transition from bridging to threefold/atop sites at high coverages that was observed for Pd(111) (Fig. 2) is not observed on smaller particles whereas it is visible to a certain extent on the larger particles indicating that larger particles have more ⟨111⟩ like character and consist of large and ordered terraces which enable the formation of a compressed and an ordered CO adsorption overlayer.[126]

3.3. NO adsorption on Pd single crystals

3.3.1. NO/Pd(111). NO adsorption on Pd(111) has been investigated extensively in the previous reports using vibrational spectroscopic techniques.[8,55,56,58,73,75,84,106,134] As in the case of CO/Pd(111) system, NO also forms various coverage-dependent ordered overlayers on Pd(111). In the literature, a c(4 × 2) phase at θ_{NO} = 0.5 ML,[8,58,75,134] which transforms into another ordered phase with a c(8 × 2) structure at θ_{NO} = 0.625 ML (ref. 8) was reported in addition to the p(2 × 2) overlayer at the saturation NO coverage of θ_{NO} = 0.75 ML.[8,58,75] Besides these ordered NO phases, another overlayer structure which lacks long range order was also reported for low NO coverages (θ_{NO} = 0.33 ML).[58,75,134] However there has been a long standing controversy regarding the adsorption site assignments for these NO overlayers using vibrational spectroscopic techniques.[73] For instance, the adsorption sites for the c(4 × 2) structure which was originally assigned to the bridging[8,58,75] sites were assigned to atop sites in a later study[106] whereas some DFT studies proposed that NO occupies threefold hollow[117] or threefold hollow + atop[76] sites in this phase.

A recent study by Hansen and coworkers[76] combining atomic resolution STM and DFT calculations seems to resolve this long standing controversy. Employing these two powerful methods, the authors suggest that NO molecules reside on the threefold hollow (fcc and hcp) sites in the c(4 × 2)–2NO domains while in the c(8 × 2)–5NO domains the NO overlayer unit cell consists of four NO molecules occupying fcc and hcp threefold sites in addition to one NO molecule on the atop sites (Fig. 1). The authors also suggest that NO molecules on the atop sites are tilted with respect to the surface normal in the c(8 × 2)–5NO phase. For the p(2 × 2)–3NO domains a unit cell structure is proposed in which one NO molecule occupies atop sites on Pd(111) with a tilted orientation in addition to two other NO molecules sitting on the 3-fold hollow sites (fcc and hcp). Another very important aspect of the NO/Pd(111) adsorption system discussed in this work is the simultaneous coexistence of different ordered NO overlayers on the Pd(111) surface. It was shown with STM[76] that at a coverage regime where a complete c(8 × 2)–5NO overlayer is expected, NO molecules *always* exist on Pd(111) as separate domains of c(8 × 2)–5NO, c(4 × 2)–2NO and p(2 × 2)–3NO. This observation was explained using adsorption energetics of different NO overlayers. Due to the repulsive interaction between the adsorbed NO molecules on the Pd(111) surface, the NO chemisorption potential energy is found to be monotonically decreasing with increasing coverage.[76] Hence it follows that the NO chemisorption potential for p(2 × 2)–3NO phase is lower than the c(8 × 2)–5NO phase whereas the NO chemisorption potential for the c(4 × 2)–2NO structure is higher than that for c(8 × 2)–5NO domains. Thus the total energy of a NO/Pd(111) system with a complete c(8 × 2)–5NO overlayer can also be obtained by having fractional overlayers of (8 × 2)–5NO, c(4 × 2)–2NO and p(2 × 2)–3NO that simultaneously exist on the Pd(111) surface.

Vibrational spectroscopic results[8,55,58] for the NO/Pd(111) system can be interpreted more accurately in the light of the information provided by the recent STM and DFT studies[76] mentioned above. Fig. 8a[8] shows the IRAS results obtained for NO/Pd(111) system at low pressures (P_{NO} = ~1 × 10^{-6} Torr). At θ_{NO} = 0.5 ML, a LEED pattern corresponding to the c(4 × 2)–2NO structure is obtained with a N–O stretching frequency of 1620 cm^{-1}. Based on the arguments mentioned above this adsorption band can be assigned to NO molecules sitting on threefold hollow sites. With increasing NO coverage another high frequency adsorption band appears around 1734 cm^{-1} that can be assigned to NO bound to atop sites with a red shift in the NO band corresponding to threefold hollow sites to 1615 cm^{-1}. When a NO coverage of θ_{NO} = 0.625 ML is reached, a LEED pattern suggesting a c(8 × 2)–5NO phase is obtained which yields NO bands at 1744 and 1736 cm^{-1}, corresponding to atop adsorption, and two additional low frequency bands at ~1605 and 1586 cm^{-1}, corresponding to adsorption at threefold hollow sites. The c(8 × 2)–5NO phase is always reported to coexist with the c(4 × 2)–2NO and p(2 × 2)–3NO domains in recent STM studies,[76] therefore the IRA spectrum for the (8 × 2) phase should be a convolution of these three phases. This argument provides a new interpretation for this spectrum in Fig. 8a, suggesting that the shoulder at ~1605 cm^{-1} can be assigned to NO molecules residing on the threefold hollow sites of the c(4 × 2)-2NO
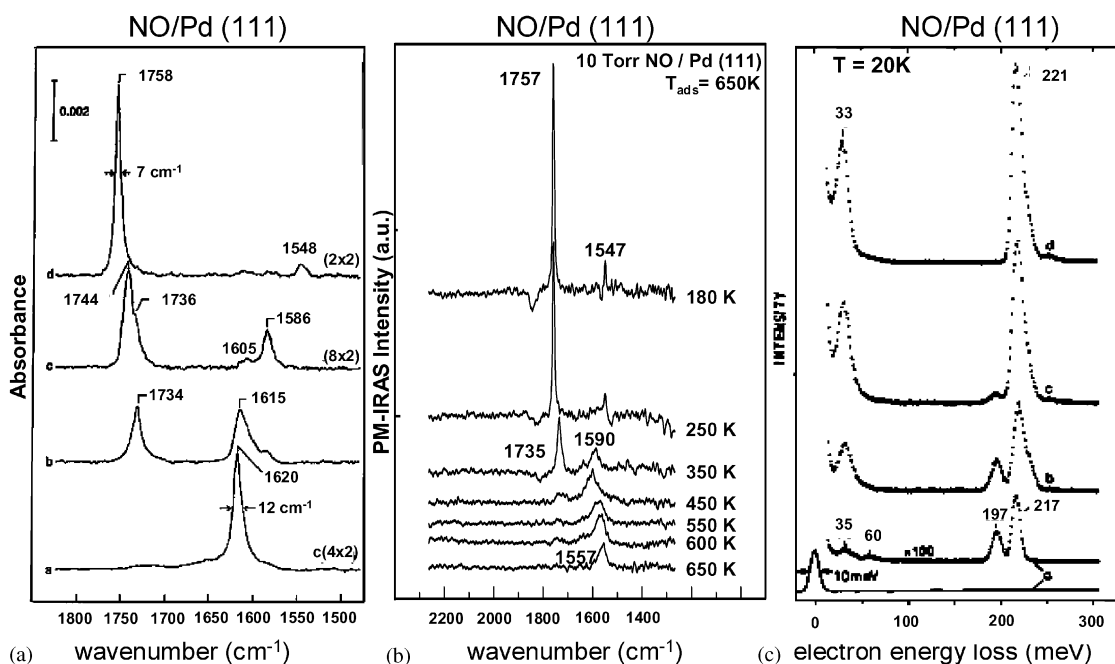
Fig. 8 (a) IRAS data representative of the ordered overlayers of NO on Pd(111) obtained at P_{NO} ~ 10^{-6} Torr 8. (b) PM-IRA spectra for NO adsorption on Pd(111) at 10 Torr.[55] (c) HREEL spectra for low temperature (20 K) NO adsorption on Pd(111) with increasing NO coverage NO-dimer formation.[58]

domains. Similarly the high frequency adsorption band at 1744 cm^{-1} can be assigned to NO species occupying atop sites of p(2 × 2)–3NO domains. The remaining two features at 1736 and 1586 cm^{-1} can be assigned to NO species adsorbed on atop and 3-fold hollow sites of c(8 × 2)-5NO domains, respectively.

At a saturation coverage of θ_{NO} = 0.75 ML, the p(2 × 2)–3NO structure is confirmed by LEED,[8] and yields two distinct NO adsorption bands in IRAS at 1758 cm^{-1} and 1548 cm^{-1}, assigned to atop and threefold hollow adsorption, respectively. The interesting aspect of the topmost IRA spectrum in Fig. 8a is the relative intensities of the NO bands bound to atop and threefold hollow sites. Since the p(2 × 2)–3NO unit cell structure implies two NO molecules adsorbed on hollow sites for every NO molecule sitting on the atop sites, the lower IRAS intensity for the multiply bonded NO species indicates significantly different IRAS cross sections for these two adsorbed states. This well known effect is demonstrated in a recent DFT study[135] where it was shown that the IR cross sections for CO molecules on atop and hollow sites of Pd(111) may vary by a factor of four as a function of the coverage-dependent overlayer structure. Fig. 8b shows the PM-IRAS results[55] for NO adsorption on Pd(111) at elevated pressures (P_{NO} = 10 Torr). It is apparent that the vibrational adsorption bands for NO follows similar trends between 10^{-6} and 10 Torr.

At lower adsorption temperatures, e.g. 20 K, in addition to the previously mentioned states, a new NO adsorption band using HREELS[134] was observed on Pd(111) at 1782 cm^{-1} (221 meV), with a shoulder at ∼1860 cm^{-1} (230 meV) (Fig. 8c). These two low-temperature features were assigned to be the asymmetric and symmetric stretchings of a weakly bound NO-dimer, (NO)$_2$, states respectively. NO-dimer states have also been observed in recent PM-IRAS studies on NO/Pd(111) system at elevated pressures.[55] Formation of NO-dimer species on Pd(111) deserves special attention as it has been shown in the literature that N$_2$O production on Ag(111) takes place via an (NO)$_2$ intermediate.[73]

NO dissociation at high temperatures (373–518 K) on Pd(111) has also been investigated by HREELS[56] and TPD[13,56] under UHV conditions. HREELS studies reveal that NO desorbs mostly molecularly from the Pd(111) surface around 500 K with a small amount of dissociation above 490 K.[56] However it was reported that NO dissociation is significantly facilitated by the stepped Pd(112) surface.[56] On the Pd(111) surface, atomic O species formed by NO dissociation is found to be stable on the surface to 550 K.[56] Above 550 K, oxygen is reported to dissolve into the bulk of Pd to form subsurface O, thus no O$_2$ species was detected in the TPD for NO desorption from Pd(111) although other desorption products such as NO, N$_2$ and N$_2$O were observed.[13,56] Other TPD experiments performed in our laboratories highlighting the significance of NO dissociation on the CO + NO reaction on Pd surfaces will be discussed in more detail in Section 3.5.

3.3.2. NO/Pd(100).
Considerably fewer studies have been reported regarding the vibrational properties of the NO/Pd(100) adsorption system[81–82,84] compared with the Pd(111) surface. HREELS results of Jorgensen and coworkers[82] are given in Fig. 9. LEED experiments reported in the same study reveal two ordered NO overlayers on Pd(100). At an NO coverage of θ_{NO} = 0.25 ML an overlayer with a p(4 × 2) structure is observed where NO occupies bridging Pd(100) sites while increasing NO coverage to θ_{NO} = 0.50 ML leads to the formation of the c(2 × 2) phase which consists of NO species bound to linear atop sites. Fig. 9 shows that a very low coverage of NO on Pd(100) leads to three loss features at frequencies at 525, 785 and 1250 cm^{-1}. Loss features at 785 and 1250 cm^{-1} were assigned to the NO dissociation products on Pd(100) whereas the feature at 525 cm^{-1} is attributed to the

background H$_2$ adsorption on Pd(100). NO dissociation has been reported to be facilitated on the open Pd(100) surface as well as on the stepped Pd single crystal surfaces whereas the Pd(111) surface was found to be relatively inactive in dissociating NO up to relatively high temperatures.[57,73] Fig. 9 indicates that at higher NO coverages on the Pd(100) surface, two other loss peaks at 1505 and 1660 cm^{-1} are observed that are suggested to correspond to NO species adsorbed on bridging and atop sites. A loss feature at 1660 cm^{-1} blue shifts with increasing coverage to 1720 cm^{-1} at saturation coverage (θ_{NO} = 0.65 ML).[82]

3.3.3. NO adsorption on Pd/Al$_2$O$_3$/NiAl(110).
Recently, Johanek and coworkers[80] have studied NO adsorption and dissociation on Pd nano-clusters with an average diameter of ∼6 nm deposited on a planar crystalline Al$_2$O$_3$ thin film grown on NiAl(110) using IRAS (Fig. 10a). Prior to NO adsorption experiments, the Pd clusters were stabilized by extensive oxygen exposure and successively treated with CO to remove surface oxygen without effecting the particle morphology.[80,136] The IRA spectrum obtained by NO adsorption at 300 K leads to three prominent vibrational features. Adsorption bands were observed at 1735 and 1595 cm^{-1} in Fig. 10b and were assigned to NO species residing on atop and 3-fold hollow sites of ⟨111⟩ facets (see also Fig. 8). The NO adsorption band at 1656 cm^{-1} was attributed to predominantly NO molecules located at particle edges with a minor contribution from NO adsorption on bridging sites of ⟨100⟩ facets (see also Fig. 9). As the temperature is increased, weakly bound atop species desorb and NO occupies only multiple coordination sites and step
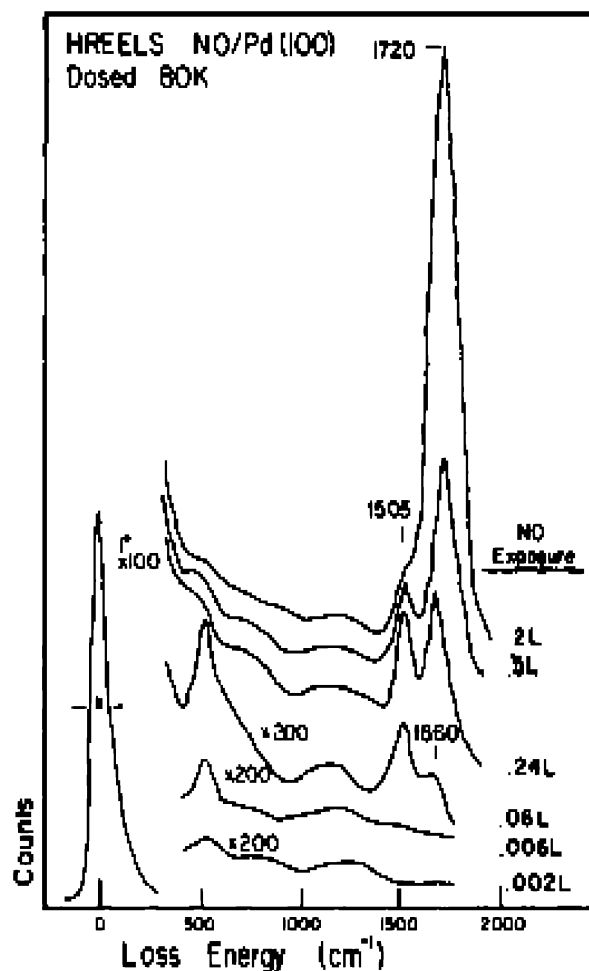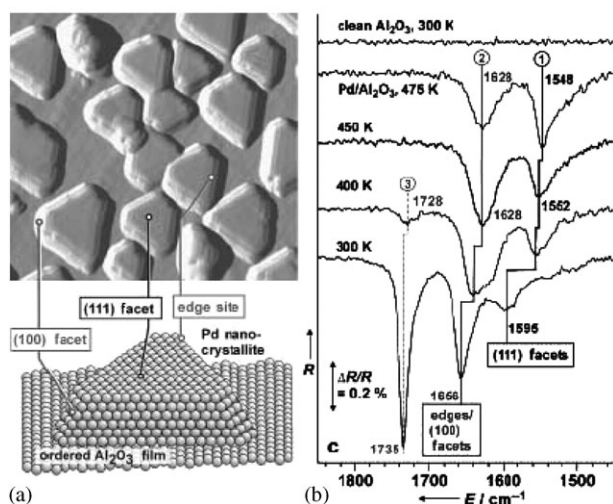

Fig. 9 HREEL spectra for NO adsorption on Pd(100) at 80 K with increasing NO coverage.[82]

Fig. 10 (a) 40 nm × 40 nm STM image for Pd particles deposited on Al$_2$O$_3$/NiAl(110) planar oxide support (top) schematic depicting the geometry of Pd particles of diameter ∼6 nm (bottom). (b) Low pressure IRA spectra for NO adsorption on Pd(6 nm)/Al$_2$O$_3$/NiAl(110) (right).[80]

edges. This is accompanied by a small red shift in the NO adsorption bands due to decreasing NO surface coverage. By monitoring the relative decrease in the intensity of NO adsorption bands at 1628 and 1552 cm^{-1} in IRAS at 450 K during NO dissociation process,[80] the authors conclude that the dissociation products (*i.e.* atomic N and O) initially block the edges or the bridging sites of ⟨100⟩ facets (1628 cm^{-1}) and subsequently block the threefold hollow adsorption sites on ⟨111⟩ facets (1595 cm^{-1}). Furthermore, it was shown that dosing pulses of CO on Pd particles at 450 K after the completion of the dissociation process leads to the evolution of CO$_2$ and removal of surface oxygen (through CO oxidation) which results in the total recovery of the band corresponding to NO adsorption on ⟨111⟩ facets while the adsorption band associated with NO adsorption on edges and ⟨100⟩ facets is partially recovered. Partial recovery of the band at 1628 cm^{-1} after CO treatment was attributed to the blocking of the edge or ⟨100⟩ sites by a strongly bound atomic N species which could not be removed by the CO oxidation reaction. In addition, the presence of such a strongly bound atomic N species on Pd particle edges was argued to enhance the rate of NO dissociation.

3.4. CO + NO coadsorption and reaction on Pd model catalysts

3.4.1. CO + NO reaction on Pd(100) and Pd(111) at low pressures.

Fig. 11a[13] presents temperature dependent IRAS results for CO + NO coadsorption on Pd(100) single crystal model catalyst surface ($P_{CO + NO} = 1 \times 10^{-6}$ Torr, $P_{CO}/P_{NO} = 1$). Two major vibrational features are observed in Fig. 11a which can be readily assigned to CO (1973-1894 cm^{-1}) and NO (1672–1630 cm^{-1}) molecules residing on the bridging sites of Pd(100) surface. Similar IRAS experiments addressing CO + NO coadsorption on Pd(111) ($P_{CO + NO} = 1 \times 10^{-6}$ Torr, $P_{CO}/P_{NO} = 1$) reveal that CO occupies predominantly 3-fold hollow sites (∼1915 cm^{-1}) in both low and high temperature conditions whereas NO prefers atop sites (1744 cm^{-1}) at low temperatures and threefold hollow sites (1576–1530 cm^{-1}) at high temperatures (Fig. 11b).[13] Furthermore at saturation coverage NO and CO bands on Pd(111) have similar intensities whereas at lower coverages NO bands have a significantly higher intensity. This is consistent with recent theoretical calculations[113] suggesting that NO has a relatively higher adsorption energy at saturation coverage with respect to CO whereas at low coverages these two adsorbates have similar adsorption energetics. It should be noted that this argument is based on the assumption that infrared intensities are proportional to the adsorbate coverage. It is known that this may not hold for certain systems in particular at high coverages due to the intensity transfer between various vibrational modes and also due to dipole–dipole coupling.[52]

IRAS data presented in Figs. 11a and 11b allow estimation of the relative surface coverage of the reactants, [NO]$_a$/[CO]$_a$, on the Pd(111) and Pd(100) model catalysts which were found to be strongly correlated to the higher activity of the former catalyst compared to the later towards CO + NO reaction. Fig. 11c[13] shows that at high temperatures ($T \geq 450$ K) where reaction starts to occur, NO is greatly stabilized on the Pd(111) surface (*i.e.* higher [NO]$_a$/[CO]$_a$) with respect to Pd(100). Implications of this observation on the kinetics of the reaction is discussed in more detail in section 3.5.

IRAS can also reveal important clues about the bonding models of CO and NO adsorbed on transition metal surfaces. The Blyholder model[70] has been widely used to interpret the frequency shifts for CO adsorption bands in vibrational spectroscopic experiments. According to this model CO binds to the metal surface *via* electron donation from its 5σ orbital that is accompanied by a back donation from the metal dπ orbital to the empty 2π* orbital of CO. As the CO coverage increases,
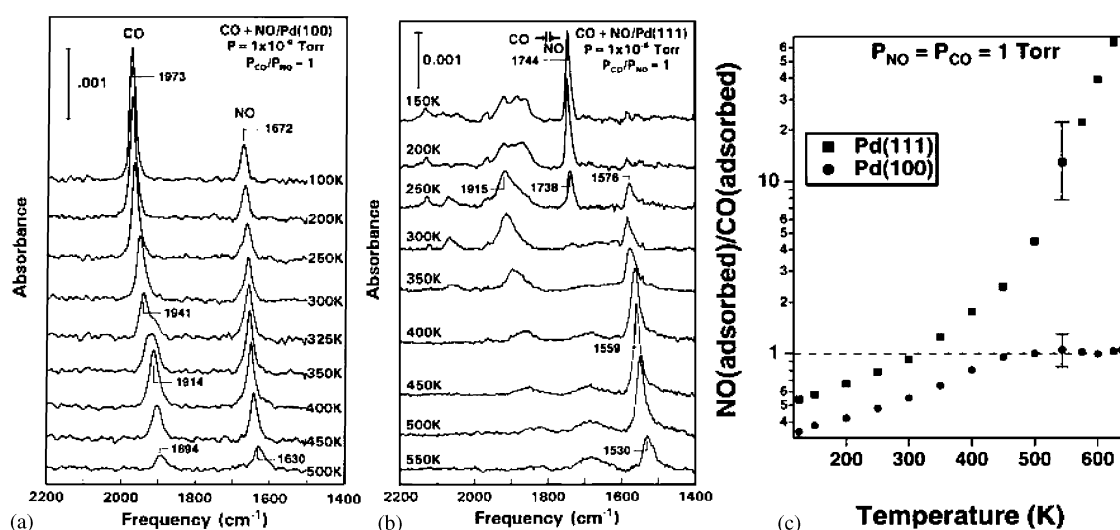

Fig. 11 Low pressure IRA spectra for CO + NO coadsorption reaction on Pd(100) (a) and Pd(111) (b) where $P_{CO+NO} = 1 \times 10^{-6}$ Torr and $P_{CO}/P_{NO} = 1$.[10] (c) Temperature dependence of [NO]$_a$/[CO]$_a$ surface coverage ratio in CO + NO reaction on Pd(111) Pd(100) where $P_{CO} = P_{NO} = 1$ Torr.[14]

depletion of the electron density of the metal d band results in decreased back donation to the 2π* orbital of CO which leads to a vibrational blue shift in the C–O stretching frequency. On the other hand, NO containing one more electron than CO in its 2π* orbital, can form a covalent bond with the metal surface through other models[37] such as spin pairing of the NO 2π* electron with a metal dπ electron to form a covalent π bond, accompanied by a donation from the NO 5σ orbital to an empty σ orbital of the metal to obtain a linear geometry. Also spin pairing of the NO 2π* electron with a metal σ electron to assume a tilted geometry where only a little donation from the NO 5σ orbital to the metal can occur. IRAS experiments[138] on CO + NO coadsorption on Pd(111) and Pd(100) at 300 K from the minimum detectable coverages to the saturation coverages indicate that the frequency shift for CO adsorption bands are +77 and +105 cm^{-1} on Pd(100) and Pd(111), respectively, whereas the corresponding shifts for NO are only +42 cm^{-1} on Pd(100) and +46 cm^{-1} on Pd(111). This marked difference in the magnitude of the coverage dependent vibrational blue shifts of NO compared to CO suggests that back donation from the metal d band to the NO 2π* orbitals may not necessarily be the prominent factor for the Pd–NO bond, however 5σ/2π* donation from NO to Pd may contribute more significantly to the observed frequency shifts. Thus with increasing NO coverage, the lesser degree of 5σ donation from NO to the metal results in only a small effect on the strength of the N–O bond as the 5σ orbital is only slightly antibonding (contrary to the CO 2π* orbital). Hence the smaller dependence of the N–O stretching frequency on Pd surfaces can be explained by stabilization of the Pd–NO bond as a result of the primarily covalent bonding interaction[137] (Besides these differences in the extent of back donation, contribution from some other less prominent factors such as differences in the extent of coverage dependent dipole–dipole coupling also play a role in the observed dissimilarities for NO and CO vibrational frequency shifts).

3.4.2. CO + NO reaction on Pd(111) at elevated pressures and the formation of isocyanate (–NCO).

Recently, the CO + NO reaction has also been studied at elevated pressures using in situ PM-IRAS.[17,21] Fig. 12a shows the PM-IRA spectra obtained in the presence of 240 mbar (i.e. 180 Torr) of CO + NO gas phase where P_{CO}:P_{NO} = 1.5. Comparison of low (Fig. 11b) and high pressure (Fig. 12a) results for CO + NO reaction on Pd(111) suggests that NO and CO occupy similar adsorption sites in both pressure regimes. Furthermore, CO$_2$ yield determined by gas phase IR spectroscopy (Fig. 12b) suggests that the reaction rate is insignificant below 550 K however above this temperature a drastic increase in the reaction rate is observed. Besides the anticipated CO and NO adsorption bands in Fig. 12a, above 500 K, development of a complex band at 2256 cm^{-1} is visible. Isotopic labeling experiments revealed that this feature is associated with an isocyanate (–NCO) containing species that is formed during the reaction of adsorbed CO and atomic N which is formed via dissociation of NO on Pd(111).[17] However, it was also reported that due to the asymmetric shape of the band at 2256 cm^{-1}, a contribution from other surface species (such as HNCO that can be formed due to surface hydrogen originating from the bulk of the Pd single crystal) cannot be excluded. The formation of the –NCO species in the reaction of CO + NO on Pd supported catalysts has also been reported to occur experimentally[89–90,139–143] and theoretically.[95] Theory suggests that the –NCO species is formed on the metal center, then spills over to the oxide support.[144] Along these lines, Solymosi and coworkers[144] reported that the vibrational features for –NCO species on supported metal particles strongly depend on the nature of the oxide but not on the type of the metal.

The formation of –NCO containing species on Pd(111) implies NO dissociation, therefore isocyanate functional group can be used as a sensitive indicator for the NO dissociation process, a crucial step in the CO + NO reaction. Detection of –NCO group at 500 K in Fig. 12a, where the CO + NO reaction is still relatively slow, suggests that NO dissociation may not be the limiting step at this temperature. A very interesting aspect of isocyanate group formation on Pd(111) at elevated pressures was demonstrated by varying the total pressure of the CO + NO gas phase (Fig. 12c).[17] It was shown that isocyanate group formation is only detected at elevated pressures (above 0.02 mbar) emphasizing the importance of in situ
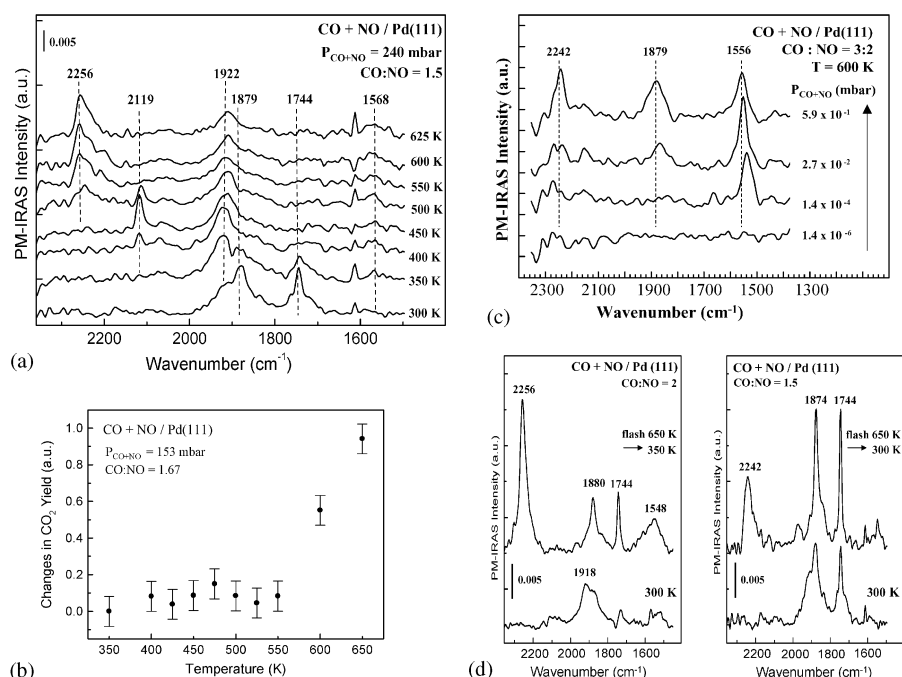
Fig. 12 (a) In situ PM-IRA spectra for CO + NO coadsorption and reaction on Pd(111) at 240 mbar (180 Torr), P_{CO}/P_{NO} = 1.5.[21] (b) Relative CO$_2$ conversion versus temperature in CO + NO reaction on Pd(111) (each data point represented here were obtained by integrating CO$_2$ yield for a period of 5 min at each given temperature).[21] (c) PM-IRAS data showing the formation of isocyanate (–NCO) group at elevated pressures.[17] (d) Influence of P_{CO}/P_{NO} partial pressure ratio on the amount of isocyanate formed on Pd(111) surface during CO + NO reaction.[21]

investigation of heterogeneous catalytic reactions under realistic experimental conditions. Furthermore, dependence of the –NCO formation on the partial pressures of the reactants in CO + NO reaction was also examined. Fig. 12d[21] shows that –NCO formation is significantly enhanced when the partial pressure of CO is increased in the reactant mixture. Besides –NCO group was found to be extremely stable on Pd(111) such that once formed at $T > 500$ K it was found to be stable between 300–650 K, even after evacuation of the reactant gases to $\sim 10^{-7}$ Torr at 300 K. In contrast, for the Rh (111) it was found that –NCO has a very short lifetime and decomposes to N_2 and CO at room temperature in the absence of an oxide support.[144]

The interesting chemistry of –NCO in the CO + NO reaction on platinum group metals deserves special attention as it was suggested that an –NCO intermediate may provide important practical improvements in catalytic NO_x abatement. Unland, et al., proposed that in the presence of excess H_2O, formation of NH_3 can also occur during the CO + NO reaction on supported Pd catalysts via hydrolysis of an –NCO intermediate.[139,140] Production of NH_3 via an –NCO intermediate during the CO + NO + H_2O reaction provides an additional route for NO_x removal by eliminating the necessity for an external reducing agent such as NH_3. Recent in situ IR studies[141] on H_2 + O_2 + CO + NO mixtures on a high surface area Pd/Al_2O_3 catalysts showed that the performance of the H_2 + O_2 + CO + NO reactant mixture is superior than the H_2O + CO + NO mixture towards NH_3 formation. Although NH_3 formation takes place through the hydrolysis of –NCO in both cases, H_2 adsorption on Pd particles was found to further weaken the N–O bond on Pd sites and thus enhance the NO dissociation process and the subsequent –NCO formation. In a related study, Cant and coworkers[142,143] demonstrated the formation of gas phase HNCO in CO + NO + H_2 reaction on high surface area Pd/SiO_2 and Pt/SiO_2 catalysts. This interesting finding supports the possibility that hydrolysis of –NCO to form NH_3 can take place via an HNCO intermediate as originally proposed by Unland.[139]

3.4.3. CO + NO reaction on Pd/SiO$_2$/Mo(110) planar model catalyst at low pressures. CO + NO coadsorption on Pd particles supported by amorphous SiO_2 thin film grown on a Mo(110) substrate yields CO and NO adsorption bands that are combination of the features observed for the separate adsorption of each reactant on the Pd(111) and Pd(100) single crystal surfaces.[36] Adsorption bands seen in Fig. 13[36] correspond to CO species located on atop (2060 cm^{-1}) and threefold hollow sites of ⟨111⟩ facets as well as on the bridging sites of ⟨100⟩ facets of the Pd particles. Beside these features NO adsorption bands associated with the atop (1735 cm^{-1}) and 3-fold hollow ($\sim$1550 cm^{-1}) adsorption on ⟨111⟩ facets in addition to bridging adsorption ($\sim$1650 cm^{-1}) on ⟨100⟩ facets is visible. It should be noted that the IRAS data presented in Fig. 13 show that at high temperatures where CO + NO reaction starts to accelerate, NO competes with CO for adsorption sites on the Pd/SiO_2 system. Under these conditions where NO dissociation is also expected to occur, NO dominates the surface and a relatively small fraction of the adsorption sites are occupied by CO molecules. The formation of –NCO has not been reported on the silica supported Pd particles of Fig. 13, likely due to the CO/NO partial pressure ratio as well as the low total pressure of the reactant mixture ($P_{CO+NO} = 1 \times 10^{-6}$) used in these experiments.

3.5. Kinetics of CO + NO reaction on Pd single crystals vs. Pd particles supported by planar high surface area oxides

Two major reaction pathways exist for the reaction of CO + NO on Pd surfaces[13,45] that dictate the selectivity of
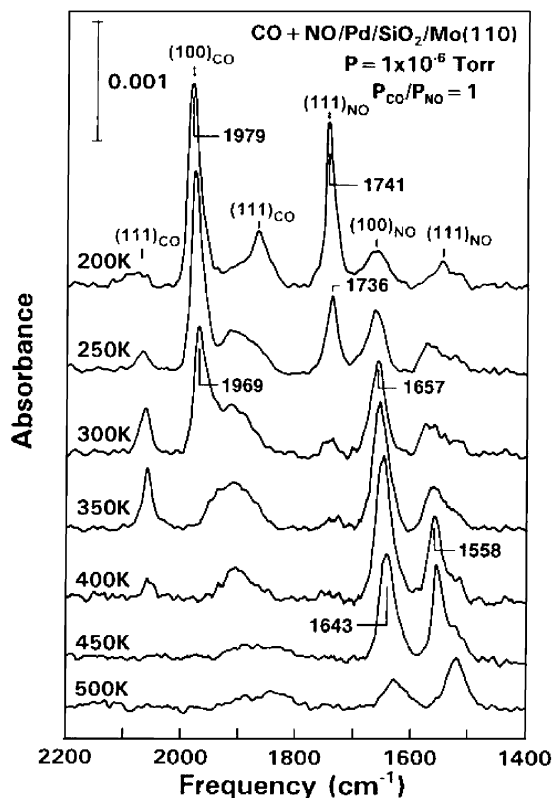

Fig. 13 IRA spectra for CO + NO coadsorption reaction on Pd(15 ML)/SiO$_2$/Mo(110) model catalyst ($P_{CO+NO} = 1 \times 10^{-6}$ Torr, $P_{CO}/P_{NO} = 1$).[10]

the reaction towards different reaction products such as N_2 or N_2O:

$$CO + NO \rightarrow CO_2 + 1/2\ N_2 \qquad (1)$$
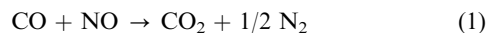
$$CO + 2\ NO \rightarrow CO_2 + N_2O \qquad (2)$$

Fig. 14a presents the combined kinetic data showing CO_2 formation rate (i.e. number of CO_2 molecules formed per active Pd site per second) as a function of inverse temperature for the reaction of CO + NO on Pd(111), Pd(100) single crystal surfaces, Pd nanoparticles deposited on a planar Al_2O_3 ultra-thin film with varying particle sizes (25 Å, 70 Å and >300 Å) in addition to conventional high surface area Pd/Al_2O_3 powder catalysts with different particle sizes (60 Å, 125 Å and 1200 Å).[44–45,133] For the Pd single crystal and planar supported model catalysts, CO + NO reaction was run in batch mode with $P_{CO} = P_{NO} = \sim$1 Torr whereas for the high surface area Pd/Al_2O_3 powder catalysts, experiments were performed using a flow reactor with $P_{CO} = 4.4$ Torr and $P_{NO} = 5.2$ Torr.[44–45,133] The most striking aspect of Fig. 14a is the strong dependence of the CO_2 formation rate on the Pd catalyst structure. According to Fig. 14a, Pd single crystal surfaces exhibit the highest activity which is followed by supported Pd particles deposited on a planar oxide while conventional high surface area Pd/Al_2O_3 catalysts show the lowest activity. A further hierarchy in the activity of the catalysts is also present within each family of catalysts given in Fig. 14a. It is apparent that the more densely packed Pd(111) single crystal surface is almost five times more active with respect to CO_2 production compared with the more open Pd(100) surface. Similarly, for the high surface area Pd/Al_2O_3 catalysts, the catalyst with Pd particles of $\sim$120 nm average diameter is about 30 times more active than the corresponding catalyst with a particle size of $\sim$6 nm. The same relationship between activity and particle size is also valid for the planar Pd/Al_2O_3/Ta(110) model catalysts although the effect is much less pronounced.
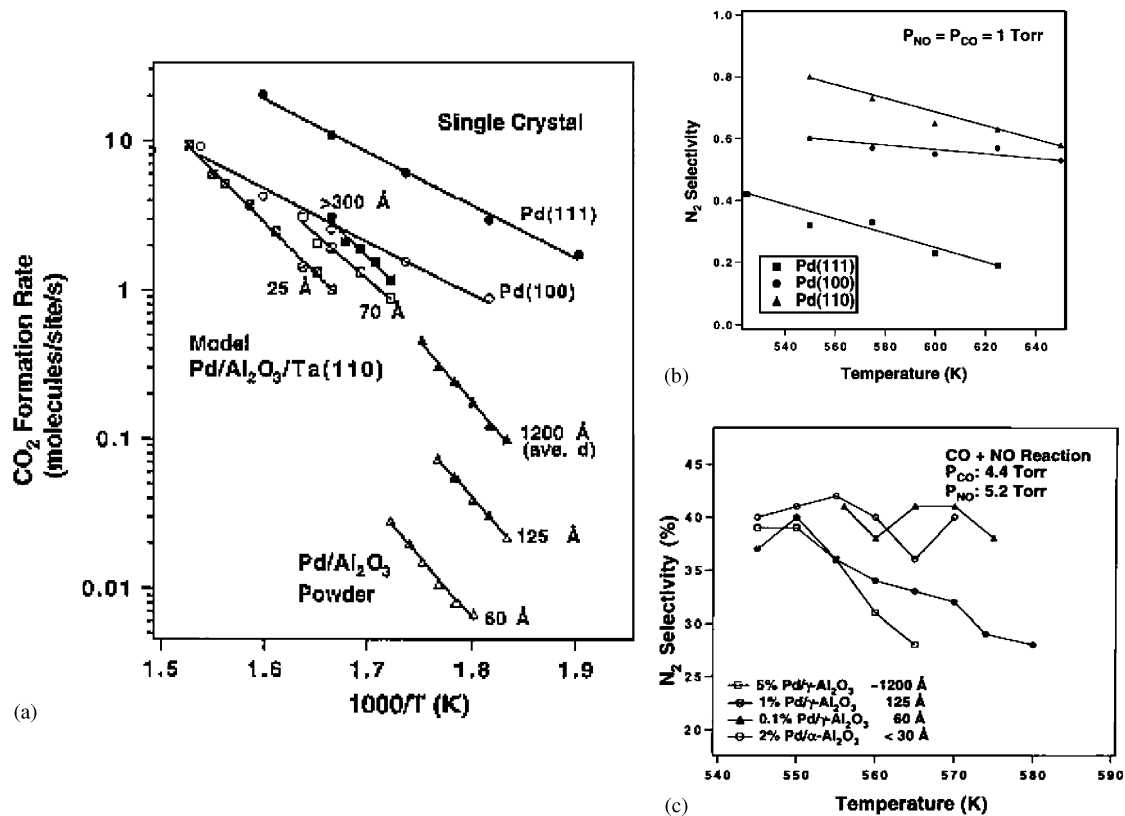
Fig. 14 (a) Structure sensitivity of CO_2 formation rate in CO + NO reaction on various Pd catalysts.(b) Temperature dependence of N_2 selectivity ($[N_2]_a/[N_2]_a + [N_2O]_a$) of CO + NO reaction on Pd single crystal model catalysts. (c) Temperature dependence of N_2 selectivity of CO + NO reaction on conventional high surface area Pd/Al_2O_3 catalysts with varying particle sizes [44]

The lower activity of the supported Pd particles on planar and high surface area oxides compared with the Pd(111) and Pd(100) single crystal surfaces is likely related to poisoning of the Pd particles by dissociation of the reactant molecules on these more highly irregular surfaces.[39] A similar explanation can be used to rationalize the difference between the activity of the planar versus high surface area supported catalysts, that is, a greater degree of order for Pd particles grown on planar oxide films result in a lower defect density and less extensive poisoning.

Since relatively large Pd particles exhibit primarily ⟨111⟩ facet orientations (Section 3.2.3), the CO + NO reaction on larger Pd particles exhibit trends observed for the Pd(111) surface. Clearly the structure sensitivity of CO + NO reaction on supported Pd particles relies on developing an understanding of those issues responsible for the differences in the catalytic activities of Pd(111) and Pd(100) single crystal model catalysts. Based on the IRAS data given in Fig. 11c, it is apparent that under the reaction conditions ($T > 500$ K), NO

is stabilized on Pd(111) more than Pd(100). Thus if NO dissociation readily occurs (*i.e.* is not rate limiting) on both of the surfaces under these conditions, the activity of the Pd(111) surface is consistent with stabilization of NO on Pd(111) to a greater extent than for Pd(100). TPD studies[44] in Fig. 15a showing the $^{15}N_2$ evolution during ^{15}NO desorption from Pd(111) and Pd(100) reveal that there are two $^{15}N_2$ desorption features in these spectra at $\sim$450 K and $\sim$550–625 K. The low temperature feature in these spectra suggests that NO dissociation (monitored by N_2 desorption) readily occurs at temperatures below the "light-off" temperature for the CO + NO reaction ($T > 500$ K) with a very small apparent activation energy for dissociation. This was also verified in PM-IRAS results at elevated pressures indicating the formation of –NCO *via* NO dissociation at $\sim$500K.[21]

The high temperature desorption feature in the TPD spectra shown in Fig. 15a suggests an inactive atomic N species which is present on the Pd(111) and Pd(100) surfaces even under reaction conditions. Comparing the total peak areas for $^{15}N_2$ desorption peaks for Pd(111) and Pd(100) suggests that NO dissociation occurs to a greater extent on Pd(100) than Pd(111), yet the Pd(100) surface is found to be still less active than Pd(111). A lower activity of the Pd(100) surface was also observed to be related to the high temperature $^{15}N_2$ desorption future in Fig. 15a as it is indicative of an inactive atomic N species which poisons the Pd(100) surface to a larger extent than that for Pd(111).[44] The existence of an inactive atomic N species on Pd surfaces was also confirmed with XPS.[44]

Temperature dependent selectivity of the CO + NO reaction on various Pd single crystal model catalysts can also be explained in the light of the IR and TPD results given above. Fig. 14b[14] reveals that the N_2 selectivity ($[N_2]/[N_2O + [N_2]$) of the Pd single crystals decrease with increasing temperature under the reaction conditions ($\sim$550–640 K). IRAS results given in Fig. 11 and PM-IRAS results for the elevated pressures presented in Fig. 12a suggest that relative $[NO]_a/[CO]_a$
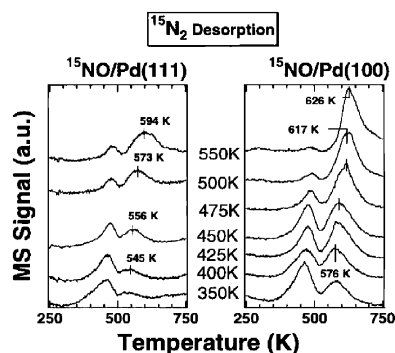
Fig. 15 TPD spectra for $^{15}N_2$ evolution during ^{15}NO desorption from Pd(111) and Pd(100).[44]

ratio for Pd single crystals is increasing with increasing temperature within 550–640 K. Thus, the second reaction pathway, *i.e.* eqn. (2), becomes more dominant as it requires stoichiometrically larger amounts of NO than the ideal reaction pathway, eqn. (1). Consequently, the second reaction pathway produces the environmentally less preferred product, N_2O, rather than N_2 and the selectivity for N_2 is observed to decrease with increasing temperature.[13,21] A similar trend for N_2 selectivity is also visible for the high surface area Pd/Al_2O_3 catalysts.[44] It has been discussed above that the stabilization of NO is greater on the Pd(111) surfaces than the Pd(100) surface. For the supported Pd particles, as the $\langle 111 \rangle$ character of the Pd particles become more significant with increasing particle size, a more significant temperature dependent decrease in the selectivity of the CO + NO reaction is observed on the larger Pd particles rather than the smaller ones.[126]

4. Conclusions

The CO + NO reaction mechanism and its kinetics on Pd surfaces were investigated using various surface science probes with emphasis on vibrational spectroscopic techniques. By scrutinizing the fundamental surface phenomena that take place on Pd single crystal model catalysts with well-defined atomically flat surfaces and Pd particles of controlled sizes deposited on planar oxide surfaces, the structure sensitivity of the CO + NO reaction on Pd surfaces is explained. Furthermore by employing *in situ* PM-IRAS technique at elevated pressures, complex model catalysts with designed properties were analyzed in real time under the conditions which are similar to the working conditions of an actual technical catalyst. Isocyanate (–NCO) group formation during CO + NO reaction on Pd(111) at elevated pressures was monitored by PM-IRAS and its implications with respect to the improvement of catalytic NO_x removal discussed.

References

1 R. M. Heck and R. J. Farrauto, *Catalytic Air Pollution Control: Commercial Technology*, International Thomson Publishing, New York, NY, 1995.
2 A. H. Tullo, *Chem. Eng. News*, 2002, **80**(34), 17.
3 B. D. Kay, C. H. F. Peden and D. W. Goodman, *Phys. Rev. B*, 1986, **34**, 817.
4 C. H. F. Peden, B. D. Kay and D. W. Goodman, *Surf. Sci.*, 1986, **175**, 215.
5 P. J. Berlowitz and D. W. Goodman, *J. Catal.*, 1987, **108**, 364.
6 P. J. Berlowitz, C. H. F. Peden and D. W. Goodman, *J. Phys. Chem.*, 1988, **92**, 5213.
7 W. K. Kuhn, J. Szanyi and D. W. Goodman, *Surf. Sci.*, 1992, **274**, L611.
8 P. J. Chen and D. W. Goodman, *Surf. Sci.*, 1993, **297**, L93.
9 J. Szanyi, W. K. Kuhn and D. W. Goodman, *J. Vacuum Sci. Technol. A*, 1993, **11**, 1969.
10 X. P. Xu, P. J. Chen and D. W. Goodman, *J. Phys. Chem.*, 1994, **98**, 9242.
11 J. Szanyi, W. K. Kuhn and D. W. Goodman, *J. Phys. Chem.*, 1994, **98**, 2978.
12 J. Szanyi and D. W. Goodman, *J. Phys. Chem.*, 1994, **98**, 2972.
13 S. M. Vesecky, P. J. Chen, X. P. Xu and D. W. Goodman, *J. Vacuum Sci. Technol. A*, 1995, **13**, 1539.
14 S. M. Vesecky, D. R. Rainer and D. W. Goodman, *J. Vacuum Sci. Technol. A*, 1996, **14**, 1457.
15 D. W. Goodman, *J. Phys. Chem.*, 1996, **100**, 13090.
16 M. Bowker, R. P. Holroyd, R. G. Sharpe, J. S. Corneille, S. M. Francis and D. W. Goodman, *Surf. Sci.*, 1997, **370**, 113.
17 E. Ozensoy, C. Hess and D. W. Goodman, *J. Am. Chem. Soc.*, 2002, **124**, 524.
18 D. C. Meier, E. Ozensoy, D. W. Goodman, in preparation.
19 A. K. Santra and D. W. Goodman, *Electrochim. Acta*, 2002, **47**, 3595.
20 E. Ozensoy, D. C. Meier and D. W. Goodman, *J. Phys. Chem. B*, 2002, **106**, 9367.
21 C. Hess, E. Ozensoy and D. W. Goodman, *J. Phys. Chem. B*, 2003, **107**, 2759.
22 C. Xu and D. W. Goodman, *Langmuir*, 1996, **12**, 1807.
23 C. Xu and D. W. Goodman, *J. Phys. Chem.*, 1996, **100**, 245.
24 C. Xu and D. W. Goodman, *J. Phys. Chem. B*, 1998, **102**, 4392.
25 J. A. Rodriguez and D. W. Goodman, *J. Phys. Chem.*, 1991, **95**, 4196.
26 J. A. Rodriguez, R. A. Campbell and D. W. Goodman, *Surf. Sci.*, 1994, **309**, 377.
27 R. A. Campbell, J. A. Rodriguez and D. W. Goodman, *Phys. Rev. B*, 1992, **46**, 7077.
28 J. A. Rodriguez, R. A. Campbell and D. W. Goodman, *J. Phys. Chem.*, 1991, **95**, 5716.
29 J. A. Rodriguez and D. W. Goodman, *Sci.*, 1992, **257**, 897.
30 G. Liu, T. P. St Clair and D. W. Goodman, *J. Phys. Chem. B*, 1999, **103**, 8578.
31 W. K. Kuhn, J. Szanyi and D. W. Goodman, *Surf.Sci.*, 1994, **303**, 377.
32 W. K. Kuhn, J. W. He and D. W. Goodman, *J. Vacuum Sci. Technol. A*, 1992, **10**, 2477.
33 P. J. Berlowitz and D. W. Goodman, *Langmuir*, 1988, **4**, 1091.
34 D. R. Rainer, J. S. Corneille and D. W. Goodman, *J. Vacuum Sci. Technol. A*, 1995, **13**, 1595.
35 X. P. Xu and D. W. Goodman, *J. Phys. Chem.*, 1993, **97**, 7711.
36 J. Szanyi, X. P. Xu and D. W. Goodman, *Abstr. Pap. Am. Chem. Soc.*, 1993, **206**, 83.
37 X. P. Xu, J. Szanyi, Q. Xu and D. W. Goodman, *Catal. Today*, 1994, **21**, 57.
38 X. P. Xu and D. W. Goodman, *Catal. Lett.*, 1994, **24**, 31.
39 E. Ozensoy, B. K. Min, A. K. Santra and D. W. Goodman, *J. Phys. Chem. B*, 2004, **108**, 4351.
40 B. K. Min, A. K. Santra and D. W. Goodman, *Catal. Today*, 2003, **85**, 113.
41 B. K. Min, A. K. Santra and D. W. Goodman, *J. Vacuum Sci. Technol. B*, 2003, **21**, 2319.
42 D. R. Rainer, M. C. Wu, D. I. Mahon and D. W. Goodman, *J. Vacuum Sci. Technol. A*, 1996, **14**, 1184.
43 D. R. Rainer, C. Xu, P. M. Holmblad and D. W. Goodman, *J. Vacuum Sci. Technol. A*, 1997, **15**, 1653.
44 D. R. Rainer, S. M. Vesecky, M. Koranne, W. S. Oh and D. W. Goodman, *J. Catal.*, 1997, **167**, 234.
45 D. R. Rainer, M. Koranne, S. M. Vesecky and D. W. Goodman, *J. Phys. Chem. B*, 1997, **101**, 10769.
46 P. M. Holmblad, D. R. Rainer and D. W. Goodman, *J. Phys. Chem. B*, 1997, **101**, 8883.
47 Y. Q. Cai, A. M. Bradshaw, Q. Guo and D. W. Goodman, *Surf. Sci.*, 1998, **399**, L357.
48 C. Xu, X. Lai, G. W. Zajac and D. W. Goodman, *Phys. Rev. B*, 1997, **56**, 13464.
49 C. Xu, W. S. Oh, G. Liu, D. Y. Kim and D. W. Goodman, *J. Vacuum Sci. Technol. A*, 1997, **15**, 1261.
50 X. Lai, T. P. St Clair, M. Valden and D. W. Goodman, *Prog. Surf. Sci.*, 1998, **59**, 25.
51 C. Xu and D. W. Goodman, *Chem. Phys. Lett.*, 1996, **263**, 13.
52 F. M. Hoffmann, *Surf. Sci. Rep. 3*, 1983, **107**.
53 D. W. Goodman, *Surf. Rev. Lett.*, 1995, **2**, 9.
54 D. W. Goodman, *Chem. Rev.*, 1995, **95**, 523.
55 E. Ozensoy, C. Hess, C. W. Yi, D. W. Goodman, in preparation.
56 R. D. Ramsier, Q. Gao, H. N. Waltenburg, K. W. Lee, O. W. Nooij, L. Lefferts and J. T. Yates, *Surf. Sci.*, 1994, **320**, 209.
57 R. D. Ramsier, Q. Gao, H. N. Waltenburg and J. T. Yates, *J. Chem. Phys.*, 1994, **100**, 6837.
58 M. Bertolo, K. Jacobi, S. Nettesheim, M. Wolf and E. Hasselbrink, *Vacuum*, 1990, **41**, 76.
59 M. Bertolo and K. Jacobi, *Surf. Sci.*, 1992, **265**, 12.
60 *Electron Spectroscopy for Surface Analysis*, ed. H. Ibach, Springer-Verlag, Berlin, New York, 1977.
61 G. A. Somorjai and K. R. McCrea, *Adv. Catal.*, 2000, **45**, 385.

62 *Vibrational Spectroscopy of Molecules on Surfaces*, ed. J. T. Yates and T. E. Madey, Plenum Press, New York, 1987.

63 T. Giessel, O. Schaff, C. J. Hirschmugl, V. Fernandez, K. M. Schindler, A. Theobald, S. Bao, R. Lindsay, W. Berndt, A. M. Bradshaw, C. Baddeley, A. F. Lee, R. M. Lambert and D. P. Woodruff, *Surf. Sci.*, 1998, **406**, 90.

64 V. V. Kaichev, I. P. Prosvirin, V. I. Bukhtiyarov, H. Unterhalt, G. Rupprechter and H. J. Freund, *J. Phys. Chem. B*, 2003, **107**, 3522.

65 M. K. Rose, T. Mitsui, J. Dunphy, A. Borg, D. F. Ogletree, M. Salmeron and P. Sautet, *Surf. Sci.*, 2002, **512**, 48.

66 G. Rupprechter, *Phys. Chem. Chem. Phys.*, 2001, **3**, 4621.

67 G. Rupprechter, H. Unterhalt, M. Morkel, P. Galletto, L. J. Hu and H. J. Freund, *Surf. Sci.*, 2002, **502**, 109.

68 S. G. Sugai, H. Watanabe, T. Kioka, H. Miki and K. Kawasaki, *Surf. Sci.*, 1991, **259**, 109.

69 S. Surnev, M. Sock, M. G. Ramsey, F. P. Netzer, M. Wiklund, M. Borg and J. N. Andersen, *Surf. Sci.*, 2000, **470**, 171.

70 G. Blyholder, *J. Phys. Chem.*, 1964, **68**(10), 2772.

71 M. R. Albert, *J. Catal.*, 2000, **195**, 62.

72 M. Bertolo and K. Jacobi, *Surf. Sci.*, 1990, **236**, 143.

73 W. A. Brown and D. A. King, *J. Phys. Chem. B*, 2000, **104**, 2578.

74 Q. Gao, R. D. Ramsier, H. N. Waltenburg and J. T. Yates, *J. Am. Chem. Soc.*, 1994, **116**, 3901.

75 H. Conrad, G. Ertl, J. Kuppers and E. E. Latta, *Surf. Sci.*, 1977, **65**, 235.

76 K. H. Hansen, Z. Sljivancanin, B. Hammer, E. Laegsgaard, F. Besenbacher and I. Stensgaard, *Surf. Sci.*, 2002, **496**, 1.

77 T. E. Hoost, K. Otto and K. A. Laframboise, *J. Catal.*, 1995, **155**, 303.

78 M. Ikai and K. Tanaka, *J. Chem. Phys.*, 1999, **110**, 7031.

79 A. J. Jaworowski, R. Asmundsson, P. Uvdal and A. Sandell, *Surf. Sci.*, 2002, **501**, 74.

80 V. Johanek, S. Schauermann, M. Laurin, J. Libuda and H. J. Freund, *Angew. Chem., Int. Ed. Engl.*, 2003, **42**, 3035.

81 C. Nyberg and P. Uvdal, *Surf. Sci.*, 1988, **204**, 517.

82 S. W. Jorgensen, N. D. S. Canning and R. J. Madix, *Surf. Sci.*, 1987, **179**, 322.

83 A. S. Mamede, G. Leclercq, E. Payen, P. Granger and J. Grimblot, *J. Mol. Struct.*, 2003, **651**, 353.

84 I. Nakamura, T. Fujitani and H. Hamada, *Surf. Sci.*, 2002, **514**, 409.

85 L. Piccolo and C. R. Henry, *Surf. Sci.*, 2000, **452**, 198.

86 R. D. Ramsier, K. W. Lee and J. T. Yates, *Surf. Sci.*, 1995, **322**, 243.

87 R. Raval, M. A. Harrison, S. Haq and D. A. King, *Surf. Sci.*, 1993, **294**, 10.

88 Y. A. Aleksandrov, I. A. Vorozheikin, K. E. Ivanovskaya and D. G. Ivanov, *Russ. J. Phys. Chem.*, 2003, **77**, 202.

89 K. Almusaiteer and S. S. C. Chuang, *J. Catal.*, 1998, **180**, 161.

90 K. Almusaiteer and S. S. C. Chuang, *J. Catal.*, 1999, **184**, 189.

91 M. Date, H. Okuyama, N. Takagi, M. Nishijima and T. Aruga, *Surf. Sci.*, 1996, **350**, 79.

92 M. Date, H. Okuyama, N. Takagi and T. Aruga, *Appl. Surf. Sci.*, 1997, **121**, 571.

93 R. Di Monte, J. Kaspar, P. Fornasiero, M. Graziani, C. Paze and G. Gubitosa, *Inorg. Chim. Acta*, 2002, **334**, 318.

94 A. Elhamdaoui, G. Bergeret, J. Massardier, M. Primet and A. Renouprez, *J. Catal.*, 1994, **148**, 47.

95 G. R. Garda, R. M. Ferullo and N. J. Castellani, *Surf. Rev. Lett.*, 2001, **8**, 641.

96 G. W. Graham, A. D. Logan and M. Shelef, *J. Phys. Chem.*, 1993, **97**, 5445.

97 M. Hirsimaki, S. Suhonen, J. Pere, M. Valden and M. Pessa, *Surf. Sci.*, 1998, **404**, 187.

98 A. S. Mamede, G. Leclercq, E. Payen, P. Granger, L. Gengembre and J. Grimblot, *Surf. Interface Anal.*, 2002, **34**, 105.

99 K. Nakao, H. Hayashi, H. Uetsuka, S. Ito, H. Onishi, K. Tomishige and K. Kunimori, *Catal. Lett.*, 2003, **85**, 213.

100 L. Piccolo and C. R. Henry, *Appl. Surf. Sci.*, 2000, **162**, 670.

101 L. Piccolo and C. R. Henry, *J. Mol. Catal. A-Chem.*, 2001, **167**, 181.

102 G. Prevot, O. Meerson, L. Piccolo and C. R. Henry, *J. Phys. Condens. Matter*, 2002, **14**, 4251.

103 G. Prevot and C. R. Henry, *J. Phys. Chem. B*, 2002, **106**, 12191.

104 M. Valden, J. Aaltonen, E. Kuusisto, M. Pessa and C. J. Barnes, *Surf. Sci.*, 1994, **309**, 193.

105 M. J. Weaver, *Surf. Sci.*, 1999, **437**, 215.

106 D. T. Wickham, B. A. Banse and B. E. Koel, *Surf. Sci.*, 1991, **243**, 83.

107 C. T. Williams, A. A. Tolia, H. Y. H. Chan, C. G. Takoudis and M. J. Weaver, *J. Catal.*, 1996, **163**, 63.

108 A. S. Worz, K. Judai, S. Abbet and U. Heiz, *J. Am. Chem. Soc.*, 2003, **125**, 7964.

109 V. P. Zhdanov and B. Kasemo, *Catal. Lett.*, 2002, **81**, 141.

110 B. Hammer and J. K. Norskov, *Adv. Catal.*, 2000, **45**, 71.

111 B. Hammer, *J. Catal.*, 2001, **199**, 171.

112 B. Hammer, *Phys. Rev. Lett.*, 2002, **89**, 16012.

113 K. Honkala, P. Pirila and K. Laasonen, *Phys. Rev. Lett.*, 2001, **86**, 5942.

114 K. Honkala, P. Pirila and K. Laasonen, *Surf. Sci.*, 2001, **489**, 72.

115 M. P. Jigato, K. Somasundram, V. Termath, N. C. Handy and D. A. King, *Surf. Sci.*, 1997, **380**, 83.

116 Z. P. Liu and P. Hu, *J. Am. Chem. Soc.*, 2003, **125**, 1958.

117 D. Loffreda, D. Simon and P. Sautet, *Chem. Phys. Lett.*, 1998, **291**, 15.

118 D. Loffreda, D. Simon and P. Sautet, *J. Chem. Phys.*, 1998, **108**, 6447.

119 D. Loffreda, D. Simon and P. Sautet, *Surf. Sci.*, 1999, **425**, 68.

120 D. Loffreda, F. Delbecq, D. Simon and P. Sautet, *J. Chem. Phys.*, 2001, **115**, 8101.

121 D. Loffreda, D. Simon and P. Sautet, *J. Catal.*, 2003, **213**, 211.

122 M. C. Asensio, D. P. Woodruff, A. W. Robinson, K. M. Schindler, P. Gardner, D. Ricken, A. M. Bradshaw, J. C. Conesa and A. R. Gonzalezelipe, *Chem. Phys. Lett.*, 1992, **192**, 259.

123 R. Raval, *Surf. Sci.*, 1995, **333**, 1.

124 J. B. Giorgi, T. Schroeder, M. Baumer and H. J. Freund, *Surf. Sci.*, 2002, **498**, L71.

125 X. P. Xu, S. M. Vesecky and D. W. Goodman, *Sci.*, 1992, **258**, 788.

126 D. R. Rainer, C. Xu and D. W. Goodman, *J. Mol. Catal. A*, 1997, **119**, 307.

127 K. H. Hansen, T. Worren, S. Stempel, E. Laegsgaard, M. Baumer, H. J. Freund, F. Besenbacher and I. Stensgaard, *Phys. Rev. Lett.*, 1999, **83**, 4120.

128 C. R. Henry, *Surf. Sci. Rep.*, 1998, **31**, 235.

129 T. Schroeder, M. Adelt, B. Richter, M. Naschitzki, M. Baumer and H. J. Freund, *Surf. Rev. Lett.*, 2000, **7**, 7.

130 T. Schroeder, J. B. Giorgi, M. Baumer and H. J. Freund, *Phys. Rev. B*, 2002, **66**art.

131 Y. D. Kim, T. Wei and D. W. Goodman, *Langmuir*, 2003, **19**, 354.

132 S. Ichikawa, H. Poppa and M. Boudart, *J. Catal.*, 1985, **91**, 1.

133 D. R. Rainer and D. W. Goodman, *J. Mol. Catal. A*, 1998, **131**, 259.

134 M. Bertolo and K. Jacobi, *Surf. Sci.*, 1990, **226**, 207.

135 A. Eichler, *Surf. Sci.*, 2003, **526**, 332.

136 I. Meusel, J. Hoffmann, J. Hartmann, M. Heemeier, M. Baumer, J. Libuda and H. J. Freund, *Catal. Lett.*, 2001, **71**, 5.

137 G. W. Smith and E. A. Carter, *J. Phys. Chem.*, 1991, **95**, 2327.

138 S. M. Vesecky, PhD Thesis, Texas A&M University, College Station, TX. 1996.

139 M. L. Unland, *Science*, 1973, **179**, 567.

140 M. L. Unland, *J. Catal.*, 1973, **31**, 459.

141 N. Macleod and R. M. Lambert, *Chem. Commun.*, 2003, 1300.

142 D. C. Chambers, D. E. Angove and N. W. Cant, *J. Catal.*, 2001, **204**, 11.

143 N. W. Cant, D. C. Chambers and I. O. Y. Liu, *Appl. Catal. B*, in press.

144 F. Solymosi and T. Bansagi, *J. Catal.*, 2001, **202**, 205.